3D printing to modulate the texture of starch-based food

Y. Bugarin-Castillo, P. Rando, M. Clabaux, G. Moulin, M. Ramaioli

3D Printing to Modulate the Texture of Starch-based Food

Y. Bugarin-Castillo[a], P. Rando[a,b] M. Clabaux[a], G. Moulin[a], M. Ramaioli[a]

[a]Université Paris-Saclay, INRAE, AgroParisTech, UMR SayFood, 91120, Palaiseau, France

[b]Department of Chemical and Process Engineering, University of Surrey, GU2 7XH, Guildford, UK

Abstract

Food 3D Printing is a novel additive manufacturing process that allows fabricating three-dimensional food products with customized shape, structure or composition. This technology was used in this study to create semi-solid bite-size food made of pre-gelatinized starch with engineered size, number of pores, and pore size. Mechanical, and geometrical properties of the prints were quantified by uniaxial compression tests and X-Ray tomography. Finally, an in-vitro set-up was used to investigate the combined effect of food hydration and uniaxial compression, in conditions inspired by tongue-palate compression.

The hydration of the starch prints leads to a drastic change in mechanical properties. Most 3D printed food designs yield and collapse under a uniaxial compression of 10 kPa, applied to mimic the squeezing of the food between the palate and the tongue. After breakage, starch dispersion increases rapidly due to the higher surface area in contact with the liquid, and the yielding point depends on the internal structure and height. Structures with a higher initial surface area in contact with the liquid have a lower yielding point, probably due to the faster hydration.

These results help understanding the dynamics of semi-solid food destructuration during oral processing and the approach developed could provide useful insights when developing food products for specific consumer needs.

Keywords: Food 3D Printing, Starch, Food Oral Processing, Food Design, Texture

1. Introduction

Food 3D Printing (3DP) is a novel fabrication technology where edible structures are manufactured with a controlled shape, size, internal structure, and texture (Prakash et al., 2019). 3DP foods are usually soft pastes made of gels and thickeners, often used to treat patients with dysphagia (Hori et al., 2015; Marconati et al., 2019; Marconati and Ramaioli, 2020). One of the drawbacks reported from patients having this disease is the loss of appetite due to unappealing food texture. 3DP allows to easily modify the texture of food products and can be used as a tool to manufacture more appealing food products (Godoi et al., 2016).

Numerous food formulations were 3D printed: starch-based products (Liu et al., 2020; Huang et al., 2019; Chen et al., 2019; Liu et al., 2018; Masbernat et al., 2021), eggs' white and yolk (Anukiruthika et al., 2020), edible gels (Liu et al., 2019; Schutyser et al., 2018; Yang et al., 2018), chocolate (Rando and Ramaioli, 2021; Mantihal et al., 2019, 2017; Lanaro et al., 2017), pectin based products (Vancauwenberghe et al., 2018), healthy snacks for children (Derossi et al., 2018) and many others. Often authors vary the texture of the food (Guénard-Lampron et al., 2021), changing the infill parameter; criterion defined in the printer software, called Slicer, which expresses the degree of internal structures of the desired product shape. Even though the infill parameter allows to easily change the food texture, it depends on the Slicer that can be different for each printer, giving poor control of the internal structure during the design phase.

Mantihal et al. (2019) and Liu et al. (2020) studied the texture attributes of 3DP foods having a different internal structure, after manufacturing. Results showed that structures with higher infill have a higher hardness and lower facturability. Due to the layer-by-layer manufacturing method, the printed structures with 100% infill showed poorer mechanical properties compared to prints prepared with the casting method. Huang et al. (2019) studied the

effect of printing parameters such as nozzle size and layer thickness on the texture of food prints made of brown rice pastes. In particular, when structures with the same shape and size are manufactured with bigger nozzle and layer thickness, the number of layers extruded is reduced leading to a change in the mechanical behavior. The hardness of the prints was found lower at a lower nozzle diameter. Furthermore, the degree of filling of a certain structure varies due to larger layers deposited in the inner part of the prints. These studies limited the investigation to determine the food texture attributes after manufacturing and did not consider the conditions of the oral phase such as the effect of food hydration, and temperature, during compression.

Mechanical compression tests are often used in the food industry to characterize the behavior of food products during the first bite. However, they can be inadequate to explain the food behavior during oral processing, which is a complex interplay of mechanical and physico-chemical phenomena. The food structure breakdown depends on the type of food (liquid, solid or semi-solid) and on the human subject (gender, age, habits) (Campbell et al., 2017). Solid and semi-solid food products, after they are introduced into the mouth, are subject to a gradual destructuration of the products and are continuously hydrated from saliva, providing lubrication until they are transformed to a bolus ready to swallow. The time needed to prepare the bolus depends on the degree of structure and on its initial water content. Also, the body temperature is approximately 37 ^{o}C and it can enhance the dissolution and dispersion of certain food components.. Soft solid foods are often squeezed between the tongue and the hard palate (Chen, 2009). The typical pressure measured during in-vivo studies was found of the order of 10 kPa (Hori et al., 2015).

The hydrolysis and dispersion of starch contained in bread products due to the action of pH and *α-amylase* during the oral and digestion phases were studied by Freitas et al. (2018) The

authors used an experimental apparatus allowing to accurately reproduce the condition of the oral and digestion phases. In the former step (set to 2.5 min) the total starch hydrolyzed varies between 2 and 20%, depending on the type of product. There are few studies reporting the dissolution of 3D printed tablets having different shapes, inner structures, and compositions, aiming to determine the drug release kinetics. Goyanes et al. (2015b, 2014, 2015a) varied the infill parameter during the manufacturing of tablets and studied the dissolution kinetics, finding that increasing the degree of filling of tablets increases the amount of drugs released. Differently from foods, the characteristic dissolution time occurring during digestion and gastric phases are significantly higher varying from minutes to hours. Moreover, tablets are generally directly swallowed, whereas food products are deconstructed in the mouth, drastically increasing the surface area in contact with the saliva and improving dispersion.

To our best knowledge, the effect of hydration was never considered during the mechanical characterization of food 3D printed products.

Based on these premises, an in-vitro apparatus was developed to study the combined mechanical and dispersion behavior of the 3D printed structures. Experimental parameters were inspired by food oral processing conditions. Food 3DP was used to manufacture starch structures having controlled size, porosity, and pore size, which varied systematically during the *in-vitro* experiments. The results of this study can be helpful for understanding the effect of food hydration on mechanical properties during food oral processing.

2. Material & Methods

2.1. Materials

Starch 1500 (Colorcon, UK) was used as a printing material. It is a partially pregelatinized maize starch in form of powder with a composition of 73% amylopectin and 27%

amylose. It has a gelatinization level of 20%, a mean particle size of 65 µm, and a moisture content of 7.2%.

Starch was mixed with deionized water (20 ±1 ^{o}C) to obtain a 30% w/w suspension. That was mixed using a magnetic stirrer (IKA RCT basic) at 850 rpm for 1 min. Afterwards, a stainless-steel spatula was used for 2 more minutes to homogenize the mixture and reduce lumps. The suspensions were used the same day to avoid any moisture evaporation.

2.2. Rheological Analysis

The rheological behavior was characterized using a PhysicaMCR-301 rheometer (Anton Paar GmbH, Germany) equipped with a parallel plate geometry (d = 25mm; gap = 1mm) at 20 and 50 ^{o}C. A frequency sweep was performed between 100 and 0.1 rad/s at 1% strain. Moreover, an amplitude sweep was performed at a constant angular frequency of 10 rad/s and varying the strain from 0.1 to 100%. The stress at which the complex modulus (G*) deviates from the Linear Viscoelastic Region (LVR) was considered as the yield stress. The measurements were performed in triplicates.

2.3. Structure Design and Extrusion 3D Printing

Cubic food structures were designed to study systematically the effect of size, porosity, and pore size. Three different groups of designs were considered for this study. The first group (G1) comprises structures characterized by the same internal pattern and number of holes, but sizes varying in the range of 10 to 25 mm. The second group (G2) includes structures having the same size (20 mm) but different internal patterns and number of holes. The structures from the third group (G3) had the same external width as those in group 2, but were printed using fewer layers and therefore had a different height. The geometrical characteristics are summarized in Table 1 and complementary measurements are shown in Table A.6. Each structure was labeled

based on the length of its side (L) and the number of pores (P) (i.e. L20P4 is a print having a side of 20 mm and 4 pores).

An extrusion-based Food 3D Printer (Foodini, Spain) was used to print 3D structures made of pre-gelatinized starch. 3D structures were designed using the Foodini JavaScript Editor, which allows defining the coordinates of the 3D structures with a Java programming language. A code giving information on the specific path followed by the extruder was developed for each structure. The printing paths of the first two layers are shown in Figure A.10. Before printing, starch suspensions were loaded into the temperature-controlled printer capsule. The printing material was kept inside the capsule for 30 min at constant temperature. The uniformity was verified with a thermocouple.

The printing material was extruded from a 0.8 mm nozzle at $T_n = 46 \pm 2$ ^{o}C in an ambient temperature of 20 ^{o}C. The printer includes a cartridge that moves the syringe at a set printing velocity $V_p = 0.3$ *mm/s* with a volumetric flow rate of $Q = 0.8$ mm^3/s along the X and Y axes. All structures were printed continuously: the extruder moves while starch is deposited without interruption.

2.5. Geometrical Characterization

After printing, images of the top (x-y plane) and lateral (z-x plane) views of the prints were taken using a camera (BASLER, Germany), with a 75 µm resolution. Moreover, measurements of the prints length, width, height, and pore size were taken manually using a caliper.

A Desktom 130 X-ray micro-computed tomography (µ-CT RX Solutions, Chavanod, France) was used to measure the 3D microstructure of the printed structures. The X-ray source

settings were: voltage of 50 kV, current source of 160 µA, and a power of 8 W. Slices were acquired with an image resolution of 20.03 µm, while the prints were rotated 180° at a step of 0.3^{o}.

The reconstructed images were analyzed using the Simpleware SCANIP software (Synopsys, Mountain View, CA, USA), to determine the structure porosity and surface area. Images were treated with median filtering and greyscale thresholding. The porosity (Φ) was defined as the ratio between the void volume and the total volume of the structure's external envelope (Eq. 1).

$$\Phi = \frac{V_{voids}}{V_{tot}} = \frac{V_{tot} - V_{starch}}{V_{tot}} \quad (1)$$

Where V_{tot}, V_{starch}, V_{voids} are respectively the total volume of an enclosing cube, the volume of printed starch and the voids' volume. V_{voids} takes into account only the open pores and was obtained from the difference between V_{tot} and the volume of starch. Furthermore, the surface area (A_s) is defined as the total interfacial area between starch and air. The surface area, from the caliper and the Image-J measurements, was calculated as $A_s = 2 \cdot A_c + 4 \cdot A_{s,lat} + no.pores \cdot 4 \cdot L_{por} \cdot h_s$; where A_c, represents the cross-section area of the top view, $A_{s,lat}$, L_{por} and h_s are respectively the lateral surface area of the prints, the length of one pore and the height of the structure.

2.6. Uniaxial Compression

The mechanical properties of 3D printed structures were characterized using a Texture Analyzer TA.HD.Plus (Stable Micro System, UK) equipped with a 5 Kg cell and a cylindrical probe (with a flat surface and a diameter of 40 mm). The tests were performed in a force-

controlled mode at room temperature (25 ± 1 ^{o}C). The probe moves down at a pre-test speed of 1 mm/s until the trigger force of 0.05 N is reached; then, the probe moves down compressing the prints at a test speed of 2 mm/s until the imposed maximum force is reached; finally, the probe moves back to the initial position at a post-test speed of 2 mm/s. The maximum forces (F_{max}) were set in order to achieve a maximum stress of around 10 KPa, typically observed during in-vivo tongue-palate measurements (Chen, 2009). Moreover, to measure the yielding point of all the prints in wet and dry conditions, other tests were performed with maximum stress (σ_{max}) of 50 KPa.

The cross-section area (A_c) was measured from the images of the top for each print, using the ImageJ software. Each measurement was repeated three times. Since each structure has a different A_c, different maximum forces were computed and applied during the compression tests, based on the target maximum pressure, as $F_{max} = \sigma_{max} \cdot A_c$. A summary of different forces applied to each structure is reported in Table 1.

2.7. Water Hydration and Compression Tests

A novel setup was developed to investigate the coupled effect of food hydration and repeated compressions, inspired by food oral processing conditions. A sketch of the dispersion apparatus is shown in Figure 1. A heated jacketed glass vessel of 250 mL contained a cylindrical customized stand which allows supporting the printed structures while they were compressed. The conductivity was measured with an InPro 7108-25-VP Conductivity Sensor (METTLER-TOLEDO, France). The water was continuously stirred at 350 rpm to achieve a uniform concentration of the starch dispersed in the water. The customized stand has an inner diameter of 2 cm and an external diameter of 4 cm, where 1 mm holes were drilled to improve the mixing. The conductivity probe was calibrated to verify a linear relation between the starch concentration

and water conductivity, using partially pre-gelatinized maize starch (Starch 1500) in a range of starch concentrations between 0 and 0.06 m_s/m_{s0}. The measured conductivity due to starch dispersion was converted into mass fraction, using the calibration curve, reported in Figure A.11, and normalized by the maximum mass fraction of starch dispersed.

During the experiments, the jacketed vessel was filled with 150 ml of deionized water and connected to a water bath to control the temperature (37 ± 0.5 ^{o}C). The printed structures were partially immersed in deionized water. The water level reached 2 mm height measured from the center of the stand. The compression protocol begins 30s after the prints were partially immersed in the water. We consider this as the initial time of the experiments (t = 0s). The compression protocols follow the same parameters explained in section 2.6. Finally, videos were recorded during the experiments using a camera (BASLER, Germany), with a 75 µm resolution and at a frame rate of 25 Hz.

2.8. Simulated Salivary Fluid (SSF) Hydration and Compression Tests

For the purpose of simulating more closely food oral processing, two structures (L20P4, L20P49) were compressed as described in Section 2.7 but using Simulated Salivary Fluid (SSF) to imitate human saliva. These two structures were selected to consider different porosity levels, close to upper and lower limits of the range studied. Prior to commencing the study, the SSF was prepared using the method detailed by the InfoGest Consensus Method (Brodkorb et al., 2019). The salivary amylase solution was adjusted to have a final activity of 75 IU/ml by using SSF and *Bacillus sp.* salivary α−amylase in the form of a lyophilized powder (A6380, Sigma-Aldrich). Every trial contained 148.6 mL of SSF, 0.4 mL of $CaCl_2$ 0.3M and 1 mL of salivary amylase solution to achieve a final volume of 150 mL.

3. Results and Discussion

3.1. Rheological properties

The rheological properties of the printing material directly affect different steps of the 3D printing process: flow in the nozzle, stability after deposition, and layer sintering (Chaunier et al., 2021, 2019; Rando, 2021; Rando and Ramaioli, 2022). In this study, the rheological properties relative to starch paste owing through the nozzle and structure stability were evaluated at their respective temperatures.

Figure 2 shows the results of starch viscosity and storage (G') and loss (G'') moduli carried out at 20 and 50 ^{o}C, to understand the rheological behavior of the printing material in the nozzle and after deposition; whereas, the yield stress (τ_0) was estimated at 20 ^{o}C (Figure 2).

The viscosity drops from 90000 to 90 Pa · s when the angular velocity was increased from 0.1 to 100 rad/s, showing a shear-thinning behavior, which is beneficial during extrusion 3D printing since in the printer nozzle shear stress is higher. The maximum shear rate at the wall ($\dot{\gamma_w}$) was estimated considering the Rabinowitsch-Mooney equation for a Power Law fluid (Rando, 2021). Equal to 17.32s^{-1}, confirming that the rheological tests were carried out in the relevant range.

At all shear rates, the storage modulus is higher compared to the loss modulus, showing a gel-like behavior of the starch suspension. Interestingly, there is no difference in viscosity between 20 and 50 ^{o}C. A higher nozzle temperature could improve the extrusion of starch mixtures. However, increasing the temperature above 46 ^{o}C leads to drying of the starch solution and clogging of the nozzle.

The yield stress, as shown in Figure 2, was obtained considering the stress at which the complex modulus (G*) deviates from the Linear Viscoelastic Region (LVR) and is found equal to 182 ± 2 Pa. Similar results were found by Azam et al. (2018) who studied the rheological

properties of orange leather by mixing wheat starch and water at 30% w/w and finding yield stress of 139 Pa. Also Chen et al., 2019 estimated values of yield stress between 32 to 455 Pa in corn, rice, and potato starch suspensions with concentrations from 15 to 25% w/w at a temperature between 70 and 85 ^{o}C.

The maximum theoretical stable height (H_y) can be estimated from the yield stress as $H_y = \frac{\tau_0}{\rho g}$ where ρ and g are respectively the starch density and the gravitational acceleration (Rando and Ramaioli, 2021). A yield stress of 182 ± 2 Pa would allow printing simple quasi-2D wall structures with a maximum theoretical height of approximately 18 mm. However, stable prints were manufactured at a height of 25 mm. The presence of an internal structure could be beneficial to improve the distribution of the stresses and the stability of the printed structure. Drying can also increase progressively the yield stress after printing, explaining the stability observed experimentally.

3.2. Mass and Geometrical Properties of the Prints

The mass of the prints was measured after printing for each structure. The results are shown in Table 2. As expected, the mass of the prints increases when increasing the degree of filling and the size.

The dimensions of all printed geometries (length, width, height and pore size) were measured after printing using a caliper (Table A.6 and Table A.7) showing that the length and width are approximately 4-10 % higher compared to the size defined in the design phase; whereas the height of the prints is consistent with the original target. A comparison of the geometrical properties measured after deposition with image analysis and the X-ray CT (XCT) are reported in Table 3 and in Figure 3. Experimental measurements were taken i) with a caliper after printing, ii) from images taken after printing using Image-J, and iii) with XCT. From the top

view images of the prints, shown in the Table 3, it is possible to see that there is an accumulation of material on one edge for all structures. This accumulation is constant throughout the edge vertical section and it is probably caused by the continuous printing sequence. The extruder stops and starts extruding on the same x-y coordinates. Whenever the extrusion starts for each layer a small excess of starch it is deposited on the initial x-y coordinates. This creates the accumulation of starch on one edge. Changing the printing sequence aiming to begin the starch extrusion at different x-y coordinates in each adjacent layer could improve the quality of the prints.

The porosity of the structures measured with different techniques is compared Figure 3(a). Structures with a lower number of pores show a higher porosity, due to the bigger pores. Also increasing the size of the printed structures increases the porosity, owing to the rather constant thickness of the walls separating the pores. XCT and caliper results show good agreement. However, the porosity measured with the caliper and Image-J could be slightly over-estimated since only lateral measurements were taken and it was assumed that the pore cross-section is constant throughout the height. Whereas experimental results suggest that the pore cross-section is larger at the base and decreases within the height. In addition, some caliper and Image-J inconsistency may be due to a non-uniformity of the pore cross section, for some structures in groups 2 and 3.

A comparison between the surface areas is reported in Figure 3(b). The surface area increases when the size of the structure increases (G1). Moreover, XCT suggest that the surface area increases also when the number of pores increases (G2). However, too many pores result in a reducing surface in contact with air (G3). XCT measurements suggest higher surface areas than other techniques, because XCT considers correctly the roughness of the structure due to the layer-by-layer building approach. Conversely, caliper and Image-J measurements were taken

assuming that the cross-section is constant. Therefore structures are assumed to be completely smooth and the computed surface areas are underestimated compared to the final prints. XCT is therefore expected to be more accurate.

Finally, Figure 3(c) shows the specific surface area calculated as the ratio between the surface area and the mass of each structure. In general, prints with higher mass have a lower specific surface area, but the differences are not as big as the absolute differences in surface area discussed above. The structures L20P81 and L20P100 show even lower specific areas due to the tiny and partially closed pores.

3.3. Deconstruction under Compression and Hydration

3D printed starch structures manufactured with different sizes and porosity were tested with the *in-vitro* dispersion apparatus, providing compression and hydration conditions inspired by oral processing. In this section, structures from G2 were compressed at maximum stress of 10 kPa, sufficient to cause their yielding. Conversely, structures belonging to G3 did not yield at 10 kPa. For this reason maximum stress of 50 kPa was used, as indicated in Table 4.

This higher stress guaranteed yielding and a controlled dispersion of the starch. It should be noted, however, that all structures in group G3 yielded below 20kPa. For the sake of clarity, the results of G1 are not shown in this section due to different ending times; as the height increases the displacement of the Texture Analyzer probe increases.

Figure 4 reports a typical graph showing the coupled effect of starch dispersion and mechanical response over time, during the deconstruction experiments. Images of the test taken at different times are shown above the graph.

On the left axis of Figure 4, is reported the normal stress applied on the starch structure; whereas the right axis shows the increase in starch mass dispersed in water (normalized by the

total starch mass) under the combined effect of hydration. During the first compression, there is yielding at 9.8 kPa of the print (t = 2.1s) which causes the structure to fracture. After yielding (t = 8.8s) the force increases again until the maximum set point of 10 kPa is reached. At this point, the print is completely deconstructed and the amount of starch dispersed increases. Finally, the print is compressed four more times, while the amount of starch dispersed into the liquid kept increasing until the end of the experiments. Multiple compressions enhance the breakage into smaller pieces and the starch dispersion. The amount of starch dispersed in the 90 s is around 35% of the maximum amount of starch. The yielding occurs during the first 10 s, whereas the timescale of the starch dispersion is significantly longer. The increase of starch dispersed in water is almost linear, albeit some sudden increases in dispersion rate seem to occur after the second and third compression. This is probably due to the short duration of the experiments, whereas for longer times an exponential curve is expected, as found by Gao et al. (2021).

Figure 5 presents the results obtained with Group 2 and 3: (a) the mass of starch dispersed over time, (b) the mass dispersed (m_s) normalized by the total starch mass ($m_{s,0}$), (c) stress-time compression plots under hydration (first cycle) of group 2 and (d) stress-time compression plots under hydration (first cycle) of group 3.

The structures from G2 show similar yielding times (structures with the same size) and the normalized dispersion rates follow all the same master curve. However, there is a slight difference at structure L20P4, this may be due to the lower surface area in contact with the water initially as shown in Figure A.12. As the number of pores increase the structure easily hydrates internally such as L20P9 and L20P16 which could explain their faster rate of dispersion and the higher percentage of normalized starch at the end of the experiments (Table 4).

Structures from G2 disperse more rapidly when structures have more pores, (P16>P4), probably due to the higher mass. The dissolution tests of 3DP pharmaceutical tablets carried out by Goyanes et al., (2014) showed that structures with higher infill (internal structure) dissolve faster.

Structures from G3 (Figure 5) show a different behavior than G2. In G3 the structures with higher mass (L20P81 and L20P100) dispersed slower, this is probably due to their lower porosity. However, when normalized starch is compared (Figure 5 (b)) the structure L20P25, dispersed at a faster rate probably due to its higher specific surface area favouring its hydration. Also, the structure L20P25 yield at lower stress which helps to a faster breakage and dispersion. After breakage, the surface area of the starch in contact with water increases due to comminution and partial dispersion of starch. Modelling both these behaviours considering a breakage function (Chen, 2009) and a dispersion model (Gao et al., 2021) could be an interesting extension of this study.

Overall, the structures showed that the amount of starch dispersed in water starts increasing after breakage. Furthermore, the increase dispersion rate is visible upon each compression. The dispersion results from L20P49 were excluded due to an artefact in the conductivity probe, its behavior under hydrated compression is presented in Figure 5 (d).

Table 4 shows the characteristic dispersion times $t_{20,}$ when 20% of starch is dispersed, and the fraction of starch mass dispersed at the end of the experiments. Comparing the dispersion time t_{20} it is possible to see that structures with more pores have a slightly faster dispersion rate, except for L20P81 and L20P100, for which XCT showed a low porosity and surface areas, suggesting many closed pores.

Prints having the same size are characterized by almost the same t_{end}, it is possible to see that the amount of dispersed starch increases when the number of pores is higher, probably due to the higher amount of material needed to manufacture the prints. On the other hand, structures with lower porosity and higher manufacturing material showed less percentage of starch dispersed.

The amount of starch dispersed at the end of the experiments varies between 29.6% and 51.2%, depending on the structures. Freitas et al. (2018) considered the oral and gastric phase of bread digestion and reported a lower starch hydrolyzed (approx. 5%) during the oral phase (t = 2.5 min) in absence of salivary amylase, while the addition of amylase increased the amount of starch hydrolyzed to 18.5%. The different product structure, composition and protocol prevent a direct comparison with the results obtained in this study.

As explained in Section 2.8, two structures (L20P4 and L20P49) were evaluated using a Simulated Salivary Fluid (SSF) to better reproduce oral processing conditions. Figure 6 shows that no significant effect of α−amylase was observed, except a slight decrease in the young modulus of the material (initial slope). Further work should be done to develop and adapt the methodology in this study to compare 3DP structures under deconstruction using liquids with closer characteristics to human saliva.

3.4. Mechanical Properties of the 3D Printed Structure

The mechanical properties of the prints were characterized by uniaxial compression using a texture analyzer (TA). The yield point was measured by identifying the local maximum in the stress-strain curves (σ_y) at which structures begin to yield (Figure 7).

The Young modulus (E) was estimated from the linear slope of the stress-strain curve as:

$$E = \frac{\Delta F}{A_c \Delta \varepsilon} \quad (2)$$

Where F and ε are respectively the force and strain measured from the TA; whereas A_c is the initial cross-section area measured after printing using ImageJ. The same protocol was used by Vancauwenberghe et al., 2018 to characterize the mechanical properties of honeycomb and cube structures made of pectin. Data were fitted considering a range of strain Δε = [0.1 – 0.2], from the stress-strain curves reported in Figure 7 in dry conditions. In each figure, the structures were grouped aiming to compare only prints with the same number of pores or length size.

All plots show a similar trend: the stress gradually increases when the strain increases until a maximum is reached at strains between 0.2 and 0.3 where the structures yield and break. Finally, the stress keeps increasing until the maximum stress imposed by the TA protocol is reached between ε= 0.6 and 0.8. At this point, the prints are completely deconstructed under the imposed force.

Figure 8 shows the stress-time curves measured from the compression in dry conditions. All plots showed a first peak, which represents the yielding point and varies between 12 and 18 kPa, depending on the structures. After yielding, the prints are continuously compressed until the maximum force imposed from the TA is reached. Structures from Group 1 which present difference in size, show that prints with higher heights have lower yielding points. The tallest print L25P4 showed less repeatability. On the contrary, increasing the pore size in Group 2 leads to lower yielding points. In fact, structures with bigger pores have a higher void fraction. Similar behavior was reported by Huang et al. (2019), who found lower hardness in 3DP foods made of a rice paste, having a lower degree of filling. Conversely for Group 3 no significant difference was

observed when comparing dry yielding points. Probably due to their similar values of surface area with respect to G2.

All yielding properties and Young modulus were evaluated during the first compression cycle. A comparison between results in dry and wet conditions is reported in Table 5. In dry conditions, all structures yield at stresses higher than 10 kPa, varying between 12.2 and 18.3 kPa, depending on the structure's size and porosity. On the contrary, when the prints are in contact with water structures yield at significantly lower stresses varying between 8.3 and 16.6 kPa. The higher surface area in contact with the liquid could explain the lower yielding points.

Figure 9 shows that increasing the size of the structures (G1) reduces the yield point (σ_y) under dry and wet conditions. For the second group (G2), the σ_y and E increase while increasing the number of pores under dry conditions. These two effects could be due to the change in porosity in both groups. Contrarily, for group 3 (G3) no significant effect was observed in the values of σ_y and E under dry conditions regardless the change of porosity. Similar values of surface area within the group could explain this behavior.

For G2 and G3 a significant difference was observed when yielding under wet conditions. This behavior could be the higher surface area in contact with the liquid. This might explain the higher yielding points in wet conditions of structures L20P81 and L20P100. When increasing the number of pores there is no hydration in the internal structure due to the absence of voids.

Most importantly, the young modulus of structures in wet conditions was always lower compared to the values estimated in dry conditions. The addition of water, makes structures less elastic enhancing the deconstruction in mouth. In fact, in Figure 9 the values of σ_y were found significantly higher in dry conditions for all structures except for L20P81. For values of E (Figure 9(c)) structures from G1 had no significant difference between dry and wet except for L20P4.

Figure 9 (a) and (b) show a comparison between the yielding points in wet and dry conditions. The structures fracture always at lower stress when are in contact with the water, no significant differences were seen in structures L20P81 and L20P100. In dry condition, structures with higher porosities have a lower yielding points. The structure L20P100 was found to have a slightly lower yielding point than expected.

Figure 9 (d) shows a comparison between the Young Modulus (*E*) of all structures against the initial surface area in contact with the liquid. The initial contact area between the starch and the liquid was calculated as: $A_{s,s\text{-}H20} = \frac{A_{s,lat} \cdot h_{H2O}}{h_S} + A_c = \frac{(A_s - 2A_c) \cdot h_{H2O}}{h_S} + A_c$ where h_{H20} is the height of the water in contact with the starch structures equal to 2 mm. Structures with a higher surface area in contact with water seem to be less elastic. The higher surface area for moisture uptake could result in a faster mass transfer of water at the print base, facilitating the deconstruction.

4. Conclusion and Perspectives

In this study, Food 3D printing was used to manufacture starch-based structures having controlled size, porosity and pore size. A starch paste with m_s = 30% w/w showed good extrudability at a T_n = 46 ^oC and stability after deposition at room temperature due to its shear-thinning behaviour and high yield stress. Moreover, the presence of an internal design improves stability of the bite sized prints. In addition, a simple in-vitro apparatus was developed, inspired by the combined effect of tongue-palate compression and hydration to study the semi-solid food destructuration.

The geometrical and mechanical properties of the 3D bite-sized structures were quantified. The uniaxial compression in wet conditions showed significantly lower yield stress

than in dry conditions. Dry structures with higher porosity and height showed lower yielding points. After wetting, structures with higher surface area in contact with the liquid fracture at lower stress, probably due to the faster mass transfer of water at the base of the structure. Finally, after breakage of the food structure, the starch dispersion rate increases proportionally to the mass of starch present in the system for all structures, except the structures with the lowest porosity, showing slower dynamics, probably induced by the lower specific surface area.

Whilst this study did not aim to simulate food oral processing, it did contribute to understanding the deconstruction behavior of semi-solid food during an innovative approach inspired by food oral hydration. This study was limited by the lack of samples studied under simulated salivary fluid. Nonetheless, future work should focus on understanding the effect of the geometrical properties of the prints in the dispersion-deconstruction experiments. The in-vitro apparatus can be further improved to reproduce better oral conditions.

Appendix A. Additional Data

Appendix A.1. Printing Path from Foodini JavaScript

Figure A.10 reported the printing path of the first and second layers used to design the starch prints. The path was repeated several times gradually increasing the z coordinate allowing to manufacture of 3D structures.

Appendix A.2. Structure Dimensions and Mass

The dimensions of the prints measured with the caliper after manufacturing are summarized in Table A.6 and Table A.7.

Appendix A.3. Conductivity Probe Calibration

The conductivity probe was calibrated to ensure a linear relationship between the amounts of starch dispersed and water conductivity. Partially pre-gelatinized maize starch in a

range of starch concentrations between 0 and 0.06 m_s/m_{s0} was dispersed in water while the conductivity was recorded. The parameters of the calibration curve were obtained by linear fitting, finding a slope of 34.793 and an intercept of 0.532. Data shows good agreement showing an R^2 = 0.996. A comparison between the experimental results and the fitting is reported in Figure A.11.

Appendix A.4. Surface area in contact with the liquid under hydration

The initial contact area between the starch and the liquid is presented for each structure in Figure A.12.

Acknowledgement

This research did not receive any specific grant from funding agencies in the public, commercial, or not-for-profit sectors.

References

Anukiruthika, T., Moses, J.A., Anandharamakrishnan, C., 2020. 3D printing of egg yolk and white with rice flour blends. Journal of Food Engineering 265, 11.

Azam, S.M.R., Zhang, M., Mujumdar, A.S., Yang, C., 2018. Study on 3D printing of orange concentrate and material characteristics. J Food Process Eng 41, e12689.

Brodkorb, A., Egger, L., Alminger, M., Alvito, P., Assunção, R., Ballance, S., Bohn, T., Bourlieu-Lacanal, C., Boutrou, R., Carrière, F., Clemente, A., Corredig, M., Dupont, D., Dufour, C., Edwards, C., Golding, M., Karakaya, S., Kirkhus, B., Le Feunteun, S., Lesmes, U., Macierzanka, A., Mackie,

A.R., Martins, C., Marze, S., McClements, D.J., Ménard, O., Minekus, M., Portmann, R., Santos, C.N., Souchon, I., Singh, R.P., Vegarud, G.E., Wickham, M.S.J., Weitschies, W., Recio, I., 2019. INFOGEST static in vitro simulation of gastrointestinal food digestion. Nat Protoc 14, 991–1014.

Campbell, C.L., Wagoner, T.B., Foegeding, E.A., 2017. Designing foods for satiety: The roles of food structure and oral processing in satiation and satiety. Food Structure 13, 1–12.

Chaunier, L., Réguerre, A.-L., Leroy, E., 2021. Contour Fitting of Fused Filaments Cross-Section Images by Lemniscates of Booth: Application to Viscous Sintering Kinetics Modeling. Polymers 13, 3965.

Chaunier, L., Valle, G.D., Lourdin, D., Réguerre, A.-L., Cochet, K., Leroy, E., 2019. Viscous sintering kinetics of biopolymer filaments extruded for 3D printing. Polymer Testing 77, 105873.

Chen, H., Xie, F., Chen, L., Zheng, B., 2019. Effect of rheological properties of potato, rice and corn starches on their hot-extrusion 3D printing behaviors. Journal of Food Engineering 9.

Chen, J., 2009. Food oral processing—A review. Food Hydrocolloids 23, 1–25.

Derossi, A., Caporizzi, R., Azzollini, D., Severini, C., 2018. Application of 3D printing for customized food. A case on the development of a fruit-based snack for children. Journal of Food Engineering 220, 65–75.

Freitas, D., Le Feunteun, S., Panouillé, M., Souchon, I., 2018. The important role of salivary α-amylase in the gastric digestion of wheat bread starch. Food Funct. 9, 200–208.

Gao, J., Tan, E.Y.N., Low, S.H.L., Wang, Y., Ying, J., Dong, Z., Zhou, W., 2021. From bolus to digesta: How structural disintegration affects starch hydrolysis during oral-gastro-intestinal digestion of bread. Journal of Food Engineering 289, 110161.

Godoi, F.C., Prakash, S., Bhandari, B.R., 2016. 3d printing technologies applied for food design: Status and prospects. Journal of Food Engineering 179, 44–54.

Goyanes, A., Buanz, A.B.M., Basit, A.W., Gaisford, S., 2014. Fused-filament 3D printing (3DP) for fabrication of tablets. International Journal of Pharmaceutics 476, 88–92.

Goyanes, A., Buanz, A.B.M., Hatton, G.B., Gaisford, S., Basit, A.W., 2015a. 3D printing of modified-release aminosalicylate (4-ASA and 5-ASA) tablets. European Journal of Pharmaceutics and Biopharmaceutics 89, 157–162.

Goyanes, A., Robles Martinez, P., Buanz, A., Basit, A.W., Gaisford, S., 2015b. Effect of geometry on drug release from 3D printed tablets. International Journal of Pharmaceutics 494, 657–663.

Guénard-Lampron, V., Masson, M., Leichtnam, O., Blumenthal, D., 2021. Impact of 3D printing and post-processing parameters on shape, texture and microstructure of carrot appetizer cake. Innovative Food Science & Emerging Technologies 72, 102738.

Hori, K., Hayashi, H., Yokoyama, S., Ono, T., Ishihara, S., Magara, J., Taniguchi, H., Funami, T., Maeda, Y., Inoue, M., 2015. Comparison of mechanical analyses and tongue pressure analyses during squeezing and swallowing of gels. Food Hydrocolloids 44, 145–155.

Huang, M., Zhang, M., Bhandari, B., 2019. Assessing the 3D Printing Precision and Texture Properties of Brown Rice Induced by Infill Levels and Printing Variables. Food Bioprocess Technol 12, 1185–1196.

Lanaro, M., Forrestal, D.P., Scheurer, S., Slinger, D.J., Liao, S., Powell, S.K., Woodruff, M.A., 2017. 3D printing complex chocolate objects: Platform design, optimization and evaluation. Journal of Food Engineering 215, 13–22.

Liu, Z., Bhandari, B., Prakash, S., Mantihal, S., Zhang, M., 2019. Linking rheology and printability of a multicomponent gel system of carrageenan-xanthan-starch in extrusion based additive manufacturing. Food Hydrocolloids 87, 413–424.

Liu, Z., Dick, A., Prakash, S., Bhandari, B., Zhang, M., 2020. Texture Modification of 3D Printed Air-Fried Potato Snack by Varying Its Internal Structure with the Potential to Reduce Oil Content. Food Bioprocess Technol 13, 564–576.

Liu, Z., Zhang, M., Bhandari, B., Yang, C., 2018. Impact of rheological properties of mashed potatoes on 3D printing. Journal of Food Engineering 220, 76–82.

Mantihal, S., Prakash, S., Bhandari, B., 2019. Textural modification of 3D printed dark chocolate by varying internal infill structure. Food Research International 121, 648–657.

Mantihal, S., Prakash, S., Godoi, F.C., Bhandari, B., 2017. Optimization of chocolate 3D printing by correlating thermal and flow properties with 3D structure modeling. Innovative Food Science & Emerging Technologies 44, 21–29.

Marconati, M., Engmann, J., Burbidge, A.S., Mathieu, V., Souchon, I., Ramaioli, M., 2019. A review of the approaches to predict the ease of swallowing and post-swallow residues. Trends in Food Science & Technology 86, 281–297.

Marconati, M., Ramaioli, M., 2020. The role of extensional rheology in the oral phase of swallowing: an in vitro study. Food & Function.

Masbernat, L., Berland, S., Leverrier, C., Moulin, G., Michon, C., Almeida, G., 2021. Structuring wheat dough using a thermomechanical process, from

liquid food to 3D-printable food material. Journal of Food Engineering 310, 110696.

Prakash, S., Bhandari, B.R., Godoi, F.C., Zhang, M., 2019. Future Outlook of 3D Food Printing. In: Fundamentals of 3D Food Printing and Applications. Elsevier, pp. 373–381.

Rando, P., 2021. 3D Printing of Food to Study Oral Processing - University of Surrey. University of Surrey.

Rando, P., Ramaioli, M., 2021. Food 3D printing: Effect of heat transfer on print stability of chocolate. Journal of Food Engineering 294, 110415.

Rando, P., Ramaioli, M., 2022. Numerical simulations of sintering coupled with heat transfer and application to 3D printing. Additive Manufacturing 50, 102567.

Schutyser, M.A.I., Houlder, S., de Wit, M., Buijsse, C.A.P., Alting, A.C., 2018. Fused deposition modelling of sodium caseinate dispersions. Journal of Food Engineering 220, 49–55.

Vancauwenberghe, V., Delele, M.A., Vanbiervliet, J., Aregawi, W., Verboven, P., Lammertyn, J., Nicolaï, B., 2018. Model-based design and validation of food texture of 3D printed pectin-based food simulants. Journal of Food Engineering 231, 72–82.

Yang, F., Zhang, M., Bhandari, B., Liu, Y., 2018. Investigation on lemon juice gel as food material for 3D printing and optimization of printing parameters. Food Science and Technology 10.

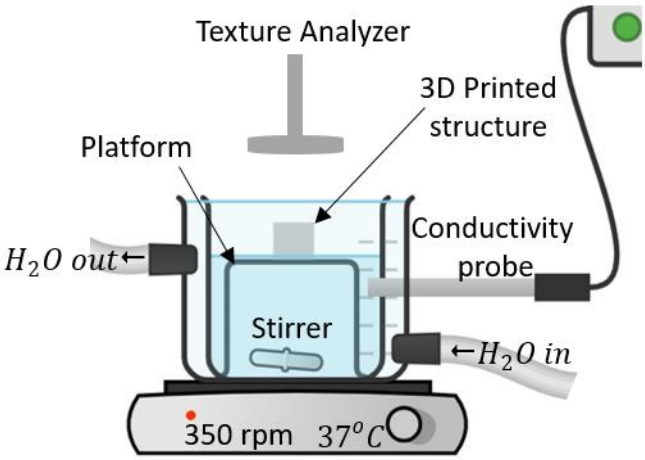

Figure 1. Sketch of the dispersion cell setup.

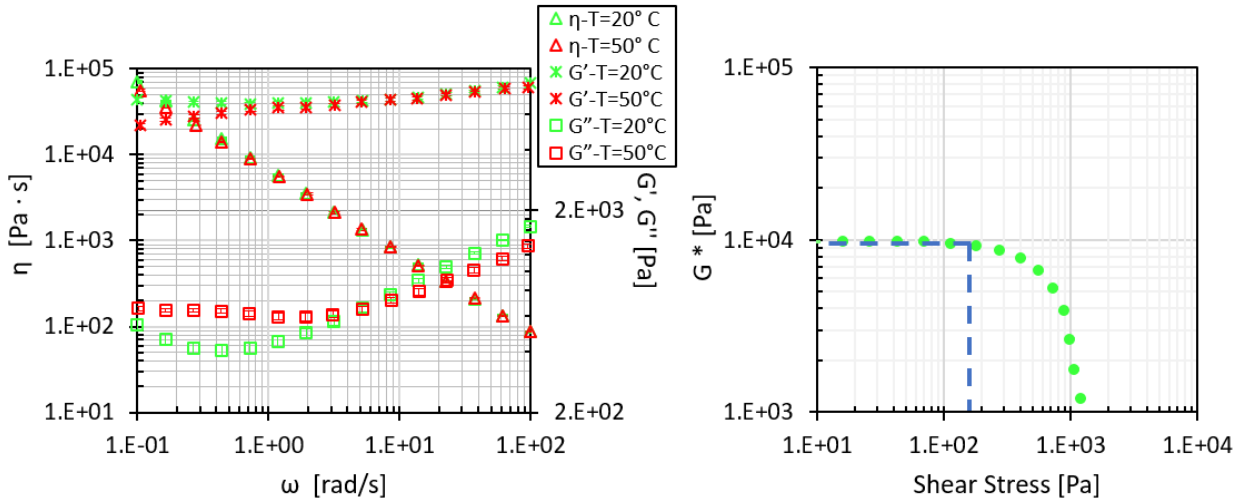

Figure 2. Rheological properties of a starch suspension at m_s =30%, measured by frequency sweep and amplitude sweep tests: (left) Complex viscosity (η), storage modulus (G'') and loss modulus (G'), (right) Yield stress τ_0 estimation at 20°C.*

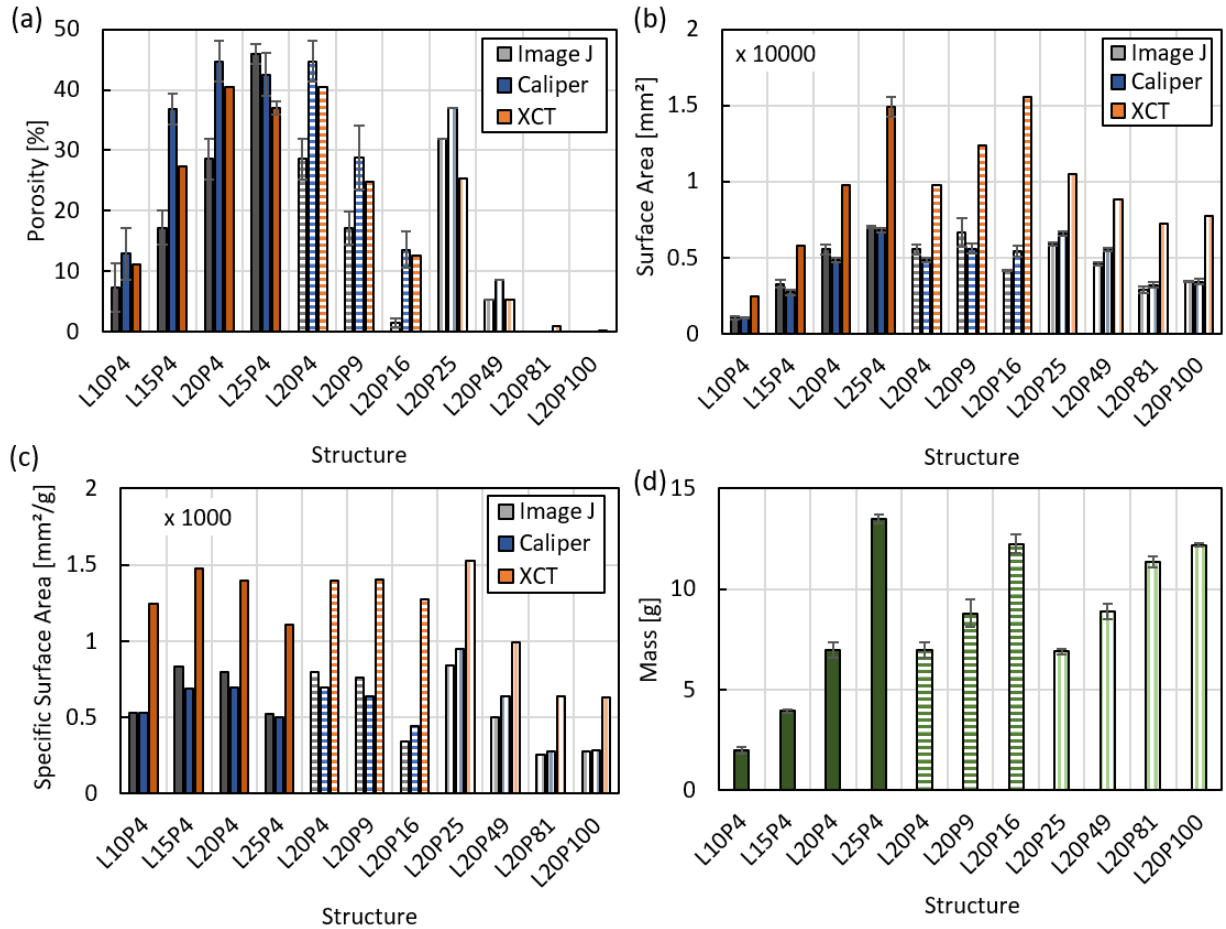

Figure 3. Comparison between measured and the design geometrical parameters for different starch structures: Image-J (gray), Caliper (dark blue), XCT (orange). (a) Porosity, (b) Surface area, (c) Specific surface area, d) Mass. Each structure was labeled based on the length of its side (L) and the number of pores (P) (i.e. L20P4 is a print having a side of 20 mm and 4 pores).

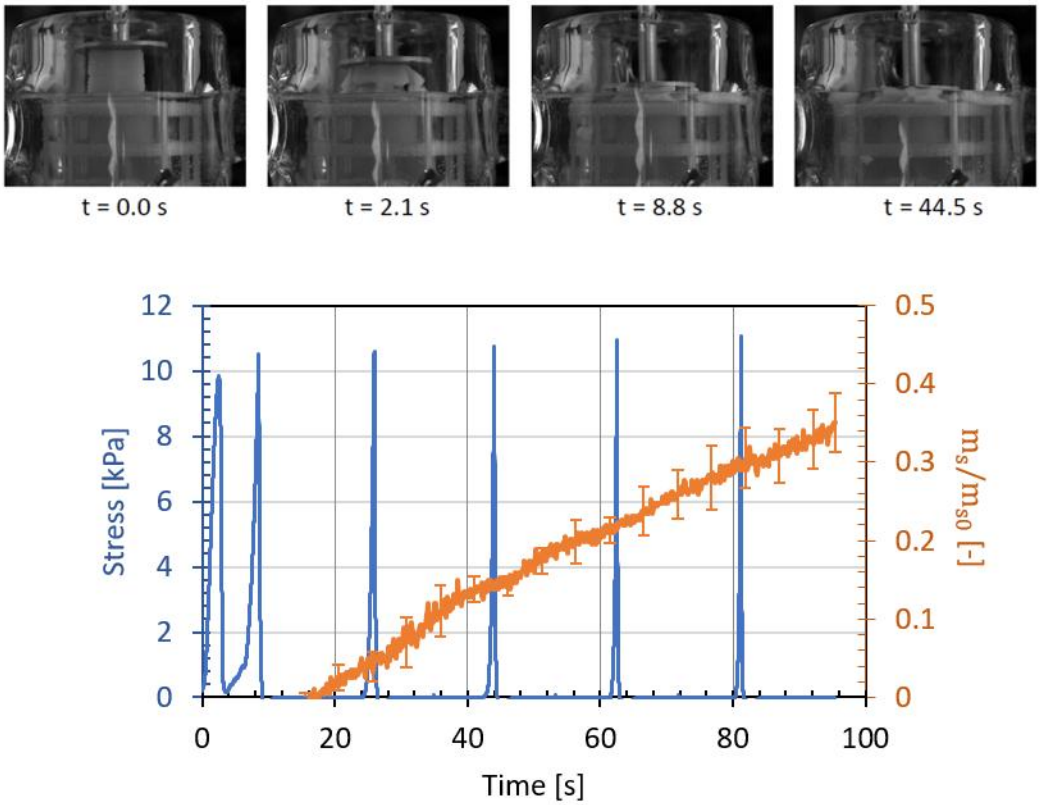

Figure 4. A typical, dispersion-compression plot of a starch 3D printed structure

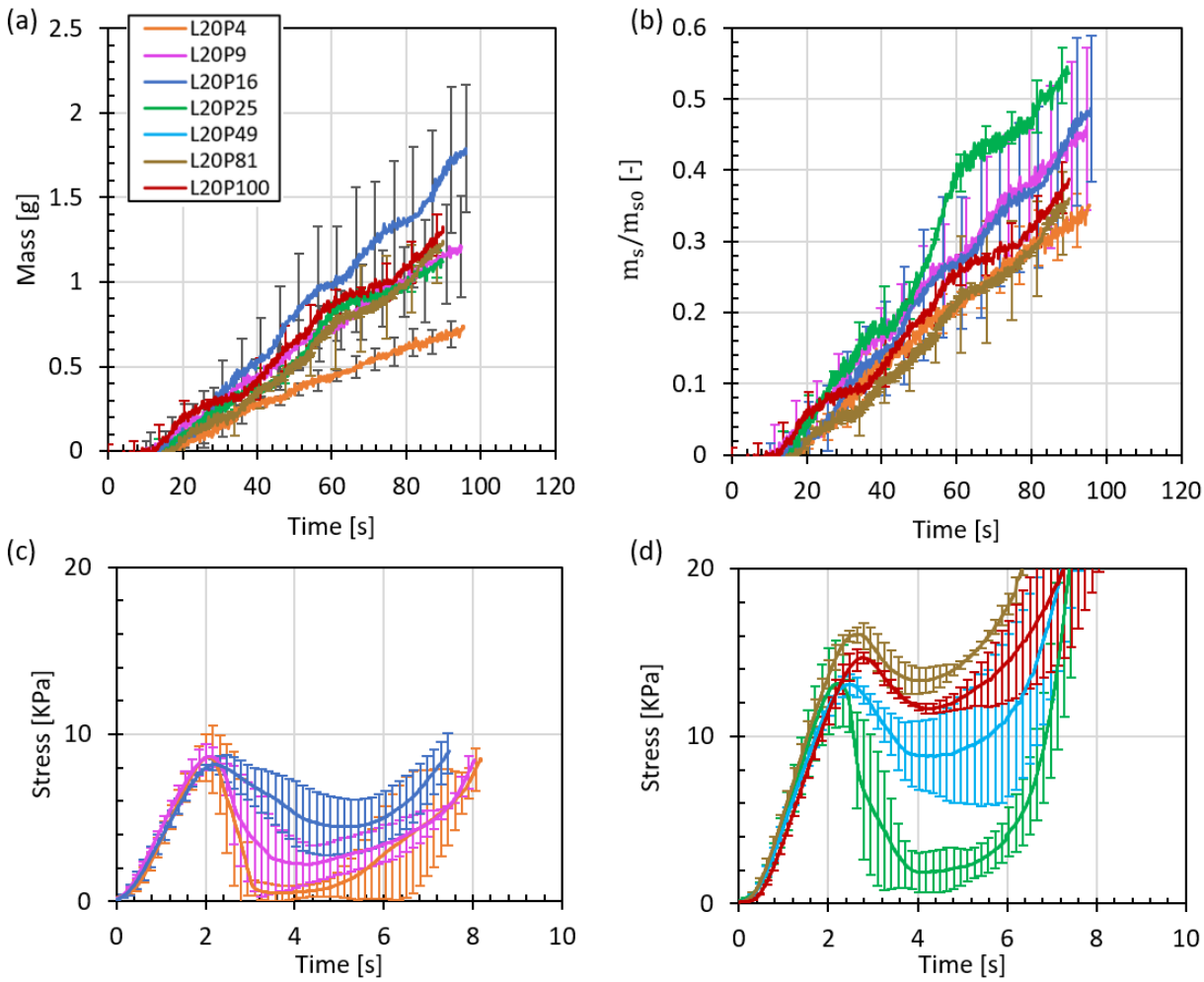

Figure 5. Group 2 under maximum stress of 10 kPa (L20P4, L20P9 and L20P16) and Group 3 under maximum stress of 50 kPa (L20P25, L20P49, L20P81 and L20P100). (a) Starch mass dispersion of the Group 2 and 3 under hydration, (b) Normalized dispersion of starch from Group 2 and 3 under hydration, (c) Stress-time plots for structures of Group 2 under hydration, (d) Stress-time plots for structures of Group 3 under hydration.

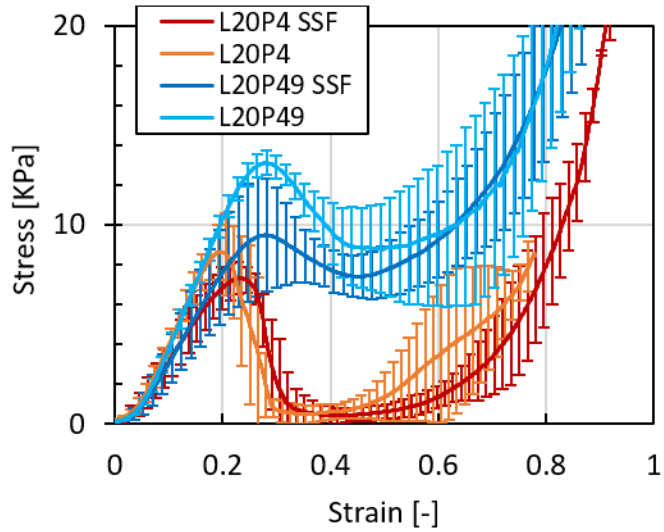

Figure 6. Stress-Strain plot under hydration with water and SSF for structures L20P4 and L20P49

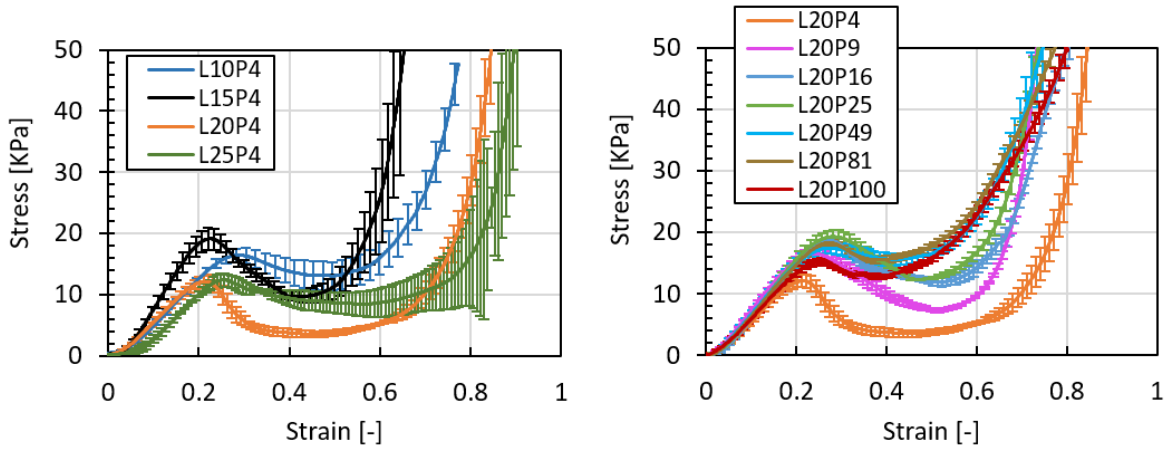

Figure 7. Uniaxial compression in dry conditions of 3DP starch structures respectively: Group 1 (L10P4, L15P4, L20P4, L25P4), Group 2 (L20P4, L20P9, L20P16) and Group 3 (L20P25, L20P49, L20P81, L20P100). (left) Stress-strain plots for structures of Group 1, (right) Stress-strain plots of structures of group 2 and 3.

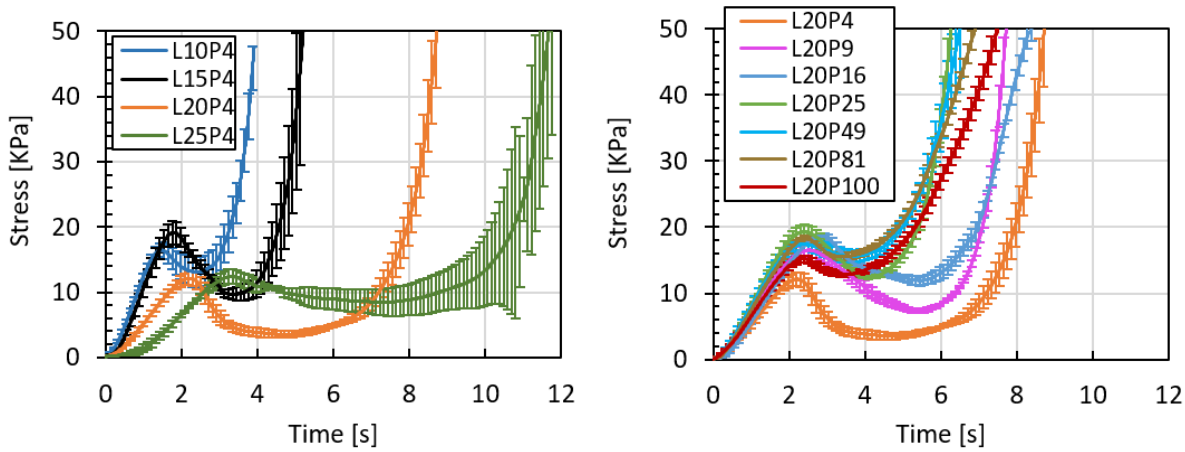

Figure 8. Mechanical behavior under uniaxial compression in dry conditions of the prints respectively: Group 1 (L10P4, L15P4, L20P4, L25P4), Group 2 (L20P4, L20P9, L20P16) and Group 3 (L20P25, L20P49, L20P81, L20P100). (Left) Stress-time plots for structures of Group 1, (right) Stress-time plots for structures of Group 2 and 3.

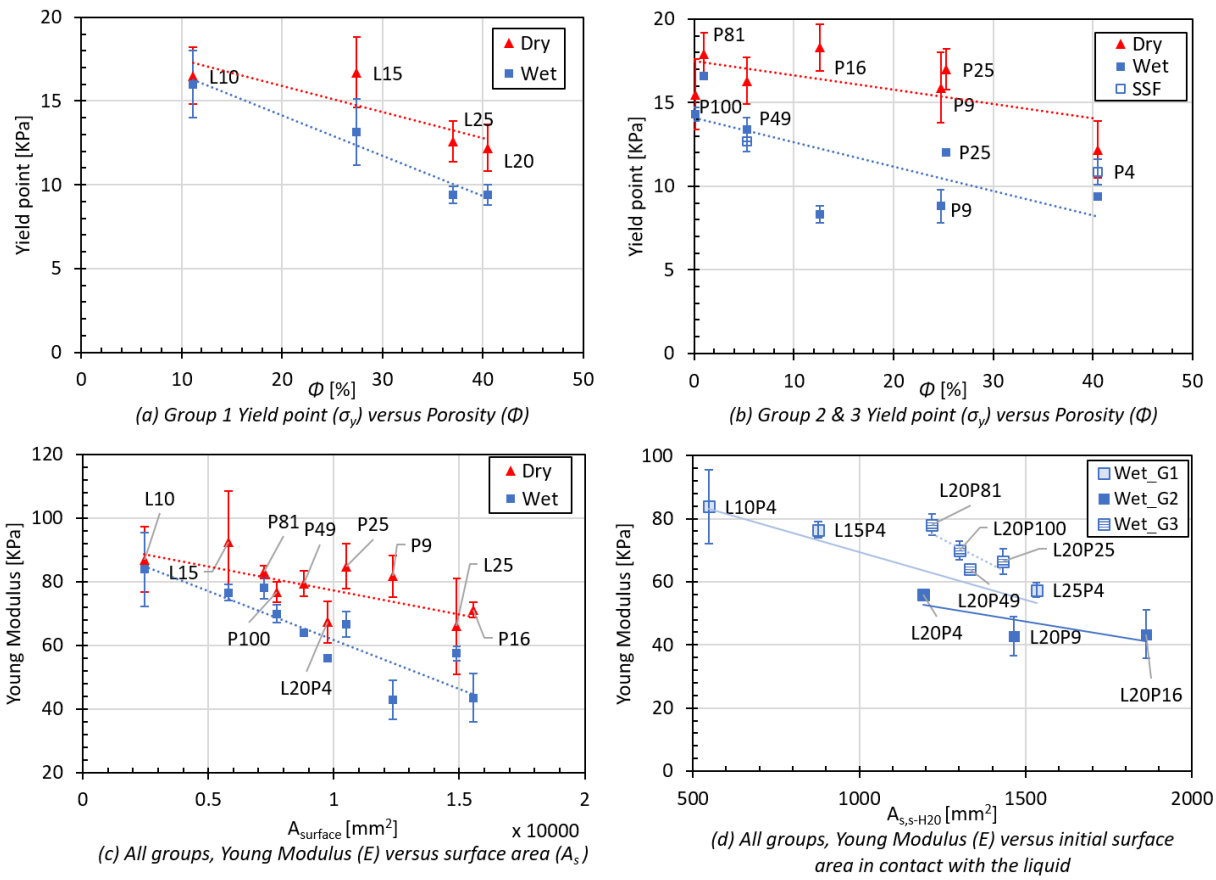

Figure 9. Comparison between yielding points in dry, water hydration conditions. The normal compression in wet conditions lowered the yielding properties of the prints. (a)Group 1 yield point (σy) versus Porosity (Φ), (b) Group 2 & 3 Yield point (σy) versus Porosity (Φ), (c) All groups, Young Modulus (E) versus surface area (As), (d) All groups, Young Modulus (E) versus initial surface area in contact with the liquid

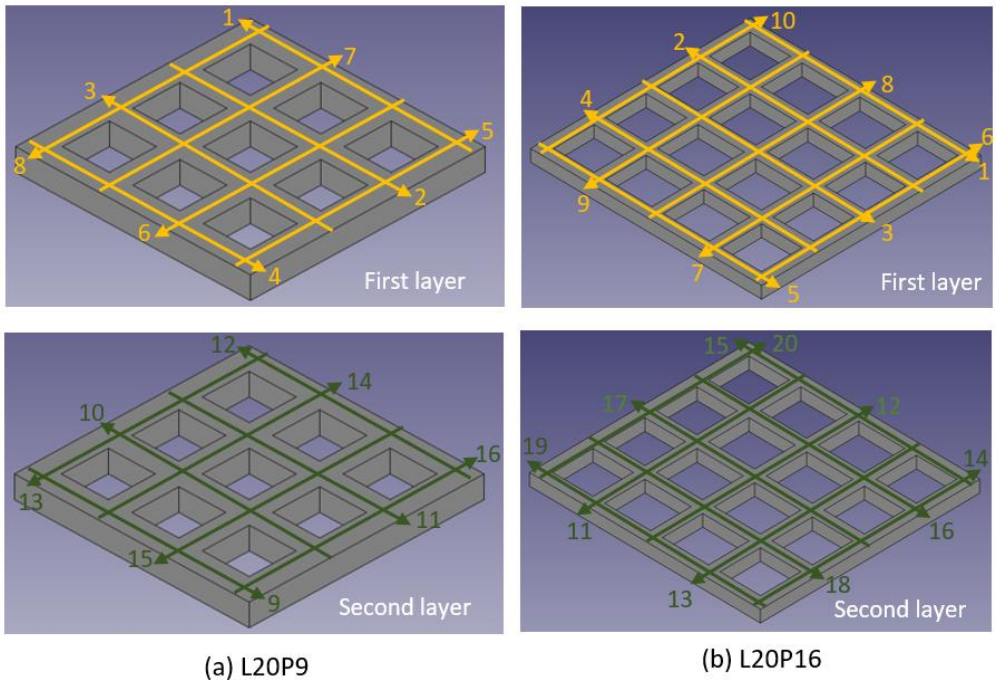

Figure A.10. Printing sequences used to print respectively the structures L20P9 and L20P16.

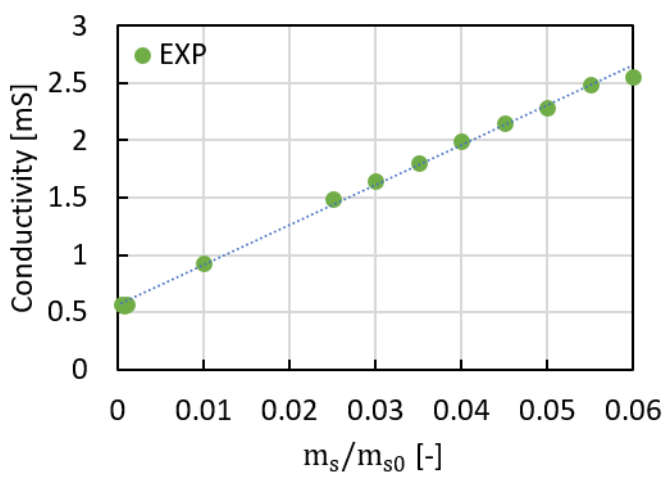

Figure A.11. Calibration curve of the conductivity probe using pre-gelatinized starch Colorcon 1500

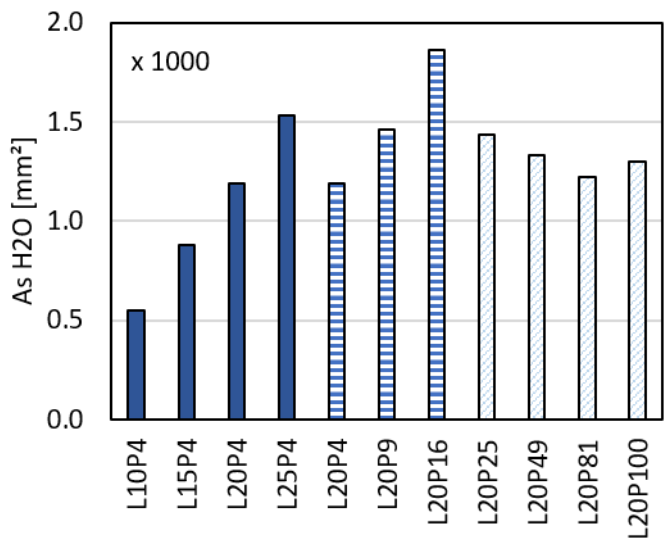

Figure A.12. Initial contact area between the starch and the liquid

Table 1. Summary of printed cubic structures, classified by the number of pores, size, and the number of layers. The measured Cross Section (Ac) and Target Maximum Forces (Fmax) computed for the compression protocol to achieve a uniaxial compression at 10 KPa and 50 KPa are listed in the last two columns.

Structure Name		No. of pores	Size (mm)	No. of layers	A_c [mm^2]	F_{max} [N]	
						σ_{max} = 10 KPa	σ_{max} = 50 KPa
G1	L10P4	4	10	25	134.8 ± 0.7	1.3	6.5
	L15P4		15	40	199.8 ± 5.1	2.0	10.0
	L20P4		20	51	288.8 ± 15.9	2.9	14.5
	L25P4		25	64	400.2 ± 38.8	4.0	20.0
G2	L20P4	4	20	51	288.8 ± 15.9	2.9	14.5
	L20P9	9			356.6 ± 18.2	3.5	17.8
	L20P16	16			437.9 ± 29.5	4.4	21.9
G3	L20P25	25	20	23	289.5 ± 7.5	2.9	14.5
	L20P49	49			433.8 ± 15.2	4.3	21.5
	L20P81	81			553 ± 7.3	5.5	27.6
	L20P100	100			590.1 ± 17.4	5.9	29.5

Table 2. Mass of the structures measured after printing

Structure Name		Mass [g]
G1	L10P4	1.97 ± 0.15
	L15P4	3.98 ± 0.09
	L20P4	6.98 ± 0.39
	L25P4	13.48 ± 0.23
G2	L20P4	6.98 ± 0.39
	L20P9	8.79 ± 0.68
	L20P16	12.25 ± 0.47
G3	L20P25	6.89 ± 0.14
	L20P49	8.88 ± 0.37
	L20P81	11.35 ± 0.28
	L20P100	12.20 ± 0.08

Table 3. Comparison of porosity and surface area of printed structures estimated using a Caliper and measured using XCT

Name	Top View Camera	XCT	Name	Top View Camera	XCT
L10P4		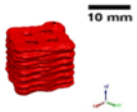	L20P9	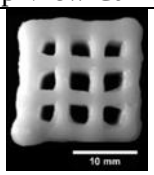	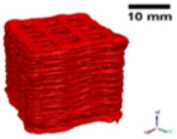
Φ [%] A_s [mm^2] V_s [mm^3]	12.95 1048.04 1218.25	11.13 2454.10 1564.01	Φ [%] A_s [mm^2] V_s [mm^3]	28.79 5593.96 7540.16	24.75 12350.47 7450.00
L15P4			L20P16	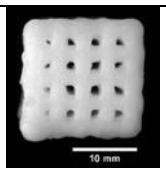	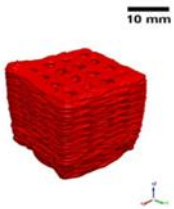
Φ [%] A_s [mm^2] V_s [mm^3]	36.82 2712.76 2792.41	27.44 5802.52 3634.89	Φ [%] A_s [mm^2] V_s [mm^3]	13.56 5411.96 8612.64	12.62 15557.86 9891.18
L20P4	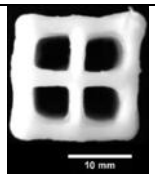		L20P25	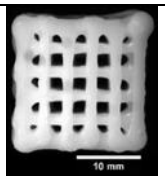	
Φ [%] A_s [mm^2] V_s [mm^3]	44.73 4848.11 5735.00	40.49 9757.74 6126.18	Φ [%] A_s [mm^2] V_s [mm^3]	36.93 6578.59 7978.37	25.32 10550.00 6595.00
L25P4	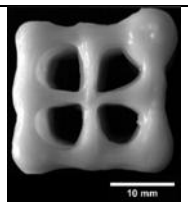		L20P49	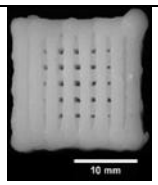	
Φ [%] A_s [mm^2] V_s [mm^3]	42.52 6807.00 8872.67	37.03 14900.00 11566.67	Φ [%] A_s [mm^2] V_s [mm^3]	8.67 5527.04 8285.88	5.27 8805.00 7290.00
L20P81	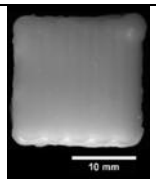		L20P100	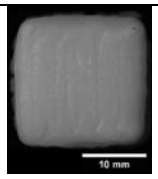	
Φ [%] A_s [mm^2]	0 3211.62	1.00 7215.00	Φ [%] A_s [mm^2]	0 3427.18	0.11 7725.00

V_s [mm^3]	9935.67	8195.00	V_s [mm^3]	10670.99	9005.00

Table 4. Characteristic dispersion times t20 when 20% of starch is dispersed and fraction of starch dispersed at the end of deconstruction and hydration experiments.

Maximum uniaxial stress [σ_{max}]	Structure name		t_{20} [s]	m_S/m_{S0} (@t_{end}) [%]
10 kPa	G2	L20P4	58.2	31.9 ± 0.0
		L20P9	46	43.9 ± 0.1
		L20P16	47	45.0 ± 0.1
50 kPa	G3	L20P25	44.4	53.7 ± 0.0
		L20P81	57.5	36.0 ± 0.1
		L20P100	52.7	38.3 ± 0.0

Table 5. Summary of Young Modulus (E) and Yield Point (σy), measured in dry and wet conditions.

Structure Name		Dry		Wet	
		σ_y [KPa]	E [Pa]	σ_y [KPa]	E [Pa]
G1	L10P4	16.5 ± 1.7	86.9 ± 10.3	16.0 ± 2.0	83.8 ± 11.7
	L15P4	16.7 ± 2.1	92.5 ± 15.9	13.1 ± 2.0	76.5 ± 2.5
	L20P4	12.2 ± 1.4	67.3 ± 6.6	9.4 ± 0.6	55.9 ± 1.0
	L25P4	12.6 ± 1.2	66.0 ± 15.1	9.4 ± 0.5	57.4 ± 2.3
G2	L20P4	12.2 ± 1.4	67.3 ± 6.6	9.4 ± 0.6	55.9 ± 1.0
	L20P9	15.9 ± 1.3	81.7 ± 6.5	8.8 ± 1.0	42.8 ± 6.1
	L20P16	18.3 ± 2.1	71.1 ± 2.3	8.3 ± 0.5	43.4 ± 7.6
G3	L20P25	17.0 ± 1.1	84.8 ± 7.1	12.0 ± 0.2	66.5 ± 4.0
	L20P49	16.3 ± 1.0	79.4 ± 4.1	13.4 ± 0.7	64.0 ± 1.0
	L20P81	17.9 ± 0.6	83.0 ± 2.1	16.6 ± 0.2	78.1 ± 3.4
	L20P100	15.5 ± 0.5	76.7 ± 3.3	14.3 ± 0.4	69.9 ± 2.9

Table A.6. Summary of the dimensions measured with the caliper after printing

Structure Name		Length [mm]	Width [mm]	Height [mm]
G1	L10P4	10.46 ± 0.44	11.48 ± 0.71	10.58 ± 0.13
	L15P4	16.74 ± 0.45	16.50 ± 0.38	15.97 ± 0.52
	L20P4	22.49 ± 0.43	22.63 ± 0.12	20.34 ± 0.42
	L25P4	26.72 ± 0.48	26.30 ± 0.23	25.47 ± 0.42
G2	L20P4	22.49 ± 0.43	22.63 ± 0.12	20.34 ± 0.42
	L20P9	22.41 ± 0.15	22.47 ± 0.09	21.02 ± 0.03
	L20916	22.00 ± 0.45	22.01 ± 0.68	20.57 ± 0.39
G3	L20P25	21.45 ± 0.19	21.42 ± 0.22	17.36 ± 0.29
	L20P49	21.72 ± 0.28	21.64 ± 0.39	17.62 ± 0.10

	L20P81	23.59 ± 0.18	23.46 ± 0.18	17.95 ± 0.11
	L20P100	24.15 ± 0.45	24.14 ± 0.43	18.29 ± 0.24

Table A.7. Summary of the dimensions measured with the caliper after printing (cont.)

Structure Name		Pore Length [*mm*]	Pore Width [*mm*]
G1	L10P4	1.96 ± 0.07	2.11 ± 0.33
	L15P4	5.02 ± 0.22	5.05 ± 0.26
	L20P4	7.54 ± 0.30	7.54 ± 0.12
	L25P4	8.62 ± 0.42	8.66 ± 0.15
G2	L20P4	7.54 ± 0.30	7.54 ± 0.12
	L20P9	4.06 ± 0.37	3.95 0.48
	L20916	2.1 ± 0.23	1.94 0.31
G3	L20P25	2.61 ± 0.03	2.61 ± 0.03
	L20P49	0.97 ± 0.08	0.94 ± 0.02
	L20P81	-	-
	L20P100	-	-